fluids

MDPI

Article

Capacity-Specific Anti-Cavitation Radial Control-Valve Trims via Density-Based Topology Optimization

Bruce Butler [1,2], Joe Alexandersen [3] and Sameer Rao [1,*]

[1] Department of Mechanical Engineering, University of Utah, 201 Presidents Circle, Salt Lake City, UT 84112, USA; bruce.butler@utah.edu
[2] Flowserve Corporation, 5215 N. O'Connor Blvd, Suite 700, Irving, TX 75039, USA
[3] Institute of Mechanical and Electrical Engineering, University of Southern Denmark, Campusvej 55, 5230 Odense M, Denmark; joal@sdu.dk
* Correspondence: s.rao@utah.edu

Abstract

We present a material distribution topology optimization (TO) framework that directly generates capacity-specific radial trims for severe-service control valves. The method uses an out-of-plane resistance modified two-dimensional turbulence model and objective functions that maximize directional change to create tortuous pressure-staging geometries at predefined channel depths. Four trims targeting non-dimensional capacities (C_V) of 0.672, 0.96 (two objectives), and 1.248 were optimized, MSLA-printed, and tested in a globe valve using IEC 60534 procedures. The measured capacities ranged from −13.7% to +4.8% of the targets for a fully 2D optimization process, dropping to a maximum of 7.8% when coupled with a hybrid 3D tuning step. Acoustic detection indicated incipient cavitation at a pressure drop ratios greater than 0.87 for the most highly staged design and 0.75 for the highest capacity design, which is consistent with our simulations of the flow field before fabrication. These results demonstrate that TO can deliver fit-to-service, capacity-tuned trims with excellent cavitation suppression, reducing reliance on large parametric design libraries.

Keywords: cavitation suppression; topology optimization; control valve; automated design

Check for updates

Academic Editors: Jinyuan Qian, Wei Dong and Zhengjing Shen

Received: 8 May 2026
Revised: 5 June 2026
Accepted: 15 June 2026
Published: 17 June 2026

Correction Statement: This article has been republished with a minor change. The change does not affect the scientific content of the article and further details are available within the backmatter of the website version of this article.

Copyright: © 2026 by the authors. Licensee MDPI, Basel, Switzerland. This article is an open access article distributed under the terms and conditions of the Creative Commons Attribution (CC BY) license.

1. Introduction

Controlling flow in cavitating and cavitation-adjacent services is of critical importance to modern industry. Such service is especially common in control valves, where internal components often see high pressure drops and other conditions that drive the fluid to vaporize in low pressure regions. When bubbles formed of this vaporized fluid move to a region of non-vaporizing static pressure, they collapse; this phenomenon is called cavitation. If the process occurs near a surface, material erosion occurs at levels proportional to the extent and energy of the cavitation. Detailed descriptions of this process can be found in several works, including [1,2]. As such erosion can quickly degrade flow control components, all major manufacturers of hydraulic flow devices are exerting significant effort to create designs which reduce or eliminate internal cavitation.

To prevent cavitation damage from occurring, the internal geometries of a severe service flow control valve (hereafter "trim" or "trim sets") are staged: the total system pressure drop is distributed over a cascade of geometrically spaced internal features. These targeted disturbances in the flow domain generate local pressure minima to reduce the number and severity of stage-downstream excursions below the fluid vapor pressure threshold. Current

practice is using shape-based parametric optimization of preidentified geometry, generally repeated elemental shapes, to achieve desired capacity and anti-cavitation performance through repeated flow analysis. Performance is generally a trade-off between achieving the required capacity, the volume of the device, and the device-specific differential pressure ratio of incipient cavitation coupled with data from the manufacturer's damage tolerance testing. In throttling service control valves, as seen in Figure 1a, these cavitation suppressing geometries are often machined into plate-style repeat units (Figure 1b) to form radial flow control mechanisms. The design of these devices often requires hundreds of flow tests and fluid simulations, and predesigned variants to meet expected use cases may stretch into thousands to meet customer demands for pressure reduction capability, overall throughput, and tailored flow control characteristics.

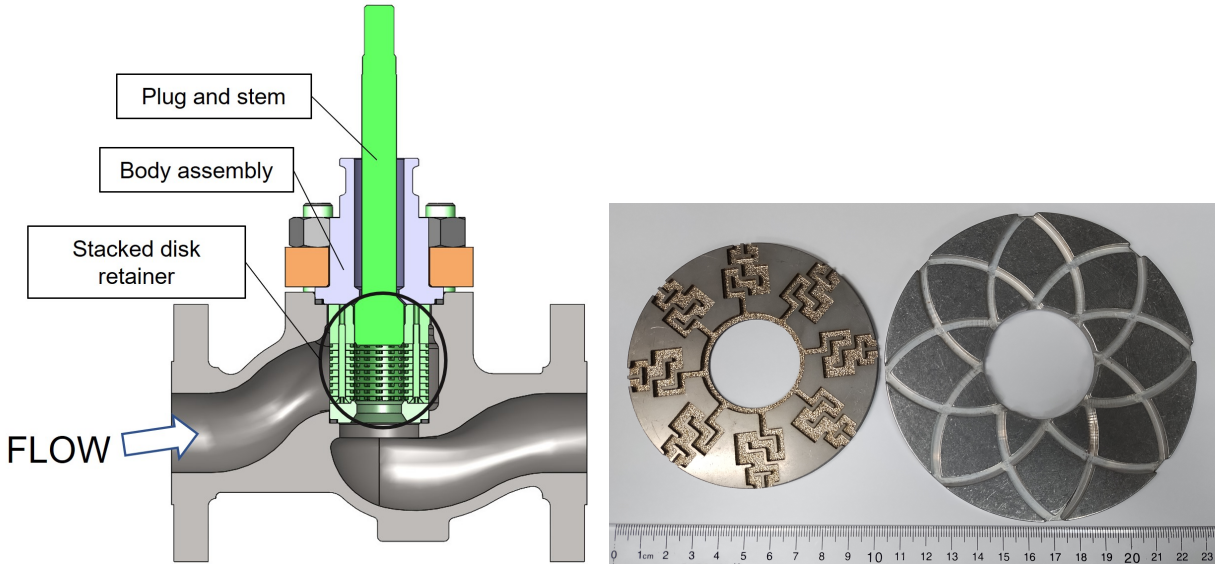


Figure 1. (**a**) Cross-section of globe-style control valve with labeled components. (**b**) Cross-section and internal cavitation suppression components of typical globe-style control valve.

Topology optimization (TO) [3,4] provides an opportunity to create design-on-demand geometries that meet customer-specific capacity and cavitation suppression requirements without the need for large design libraries. Until 2003, TO was primarily used to optimize load-bearing structures using strain energy techniques [5,6]. At that point, Borrvall and Petersson [7] demonstrated a variant of the method for use in the generation of flow geometries that used minimization of fluid power dissipation in a Stokes flow domain through a variable density field; this advancement was quickly followed by an extension to incompressible Navier–Stokes flows by Gersborg-Hansen et al. [8] and Olesen et al. [9] using the Poiseuille flow approximation and a porous medium model. TO was applied to turbulent flows by Othmer [10], without modification to the turbulence equations, and Kontoleontos et al. [11] who modified Spalart–Almaras (SA) turbulence equations to account for solids and walls. Yoon [12] performed similar work, also using SA, via finite elements. Dilgen et al. [13] presented a modified two-equation turbulence model ($k-\omega$) followed by Yoon [14] for the $k-\epsilon$ model. A more thorough review of fluid TO and its application to turbulent flow can be found in [15].

Optimizing for cavitating flow is a fraught enterprise, given that simulating the onset of cavitation is prone to gross over- and under-prediction of boundary layer pressure in separation zones and near geometric extrema [16,17]. These simulations are complex, as the phase change in the fluid is driven by properties like bubble nucleation, slip mechanics and

bubble advection, surface tension, and vapor fraction. Objectives formulated using direct calculation of minimum pressure are distorted by extremes in small pockets of solution elements. When addressing this problem, it is therefore important to choose an objective that has reduced sensitivity to local extrema and robustly converges to a valid result when coupled with the chosen flow model. Given these factors, there is very limited literature on TO for the design of cavitation suppression flow control devices. An exception is [18], in which authors used a genetic algorithm to determine the size and number of holes in a series of orifice plates and to address the design's structural strength; the work did not, however, create free-form geometry using TO.

In a previous publication [19], the authors investigated the generation of a simple single-inlet cavitation-suppressing flow device using material distribution topology optimization (TO), adjoint sensitivity analysis and gradient-based optimization. In this work, we extend these preliminary findings and demonstrate a number of fundamental improvements which are needed to design, fabricate, and test fully functional radial multi-inlet control valve cavitation suppression trim. These improvements include:

- A multi-inlet radial domain with drop-in valve compatibility;
- Seeding for flow uniformity to prevent uneven wear and orientation-dependent performance;
- Use of production-specific values to drive the generation of standardized specific-capacity designs;
- Insight into the relationship between the non-uniform hydraulic diameter and cavitation suppression performance;
- Fabrication of the commercial product compatible valve trim;
- Performance testing of the TO-enhanced control valves using standardized IEC methods.

We show that by applying TO coupled with additive manufacturing, the need for large sets of pre-configured component designs becomes unnecessary (along with the associated design and maintenance burden); generation of a specialized design and the associated analysis may become a single step that is completed as the need occurs. In addition, by choosing an objective function to drive the generation of the design rather than analyzing a pre-chosen geometry, freeform features can emerge that were previously artificially excluded from the design space.

The paper is structured as follows: Section 2 (Materials and Methods) presents the valve and flow equations required to define a useful design space, the governing equations and TO methods, and the setup and procedures used to physically validate the performance of the generated components. Section 3 (Results) details the results of the evaluation of the components, both from the hard-boundary flow analysis and the liquid capacity and noise testing. Finally, the conclusion in Section 4 summarizes the finding and impacts of this work and lays out a direction for continued development.

2. Materials and Methods

In this study, we implemented a workflow with the ability to bypass the computational hurdle of 3D optimization in a large domain with turbulent RANS, which is not feasible in a practical context. Instead of performing the hundreds of optimization iterations on a full 3D domain with resolved boundary layers (or using excessively coarse meshes which negate the additional accuracy of a 3D flow model), we introduced a two-stage TO workflow where the 2D optimization does the expensive creative work of generating the channel topology using a variable permeability model, and a subsequent simulation determines the hard-boundary threshold at the edge of the generated permeable flow path. This final simulation can be 2D or 3D depending on the desired accuracy; both are demonstrated in this work. This two-stage methodology contribution demonstrates what 2D optimization

can deliver and provides a concrete path to 3D accuracy (both are shown in this work), which is useful until large domain 3D turbulent TO becomes tractable.

As a demonstration of this workflow, we generated four unique radial anti-cavitation trim sets for a globe-style control valve. The process required the definition of a design field compatible with the footprint of the chosen control valve trim volume and the valve-specific performance targets, the generation of the optimization variables, the integration of these variables into the governing equations, and the use of a series of simulations and design updates to drive the design process. Flow and noise performance evaluations of the designs were conducted by physically testing 3D-printed components. An overview of the process can be seen in the Figure 2 flow chart and the following subsections.

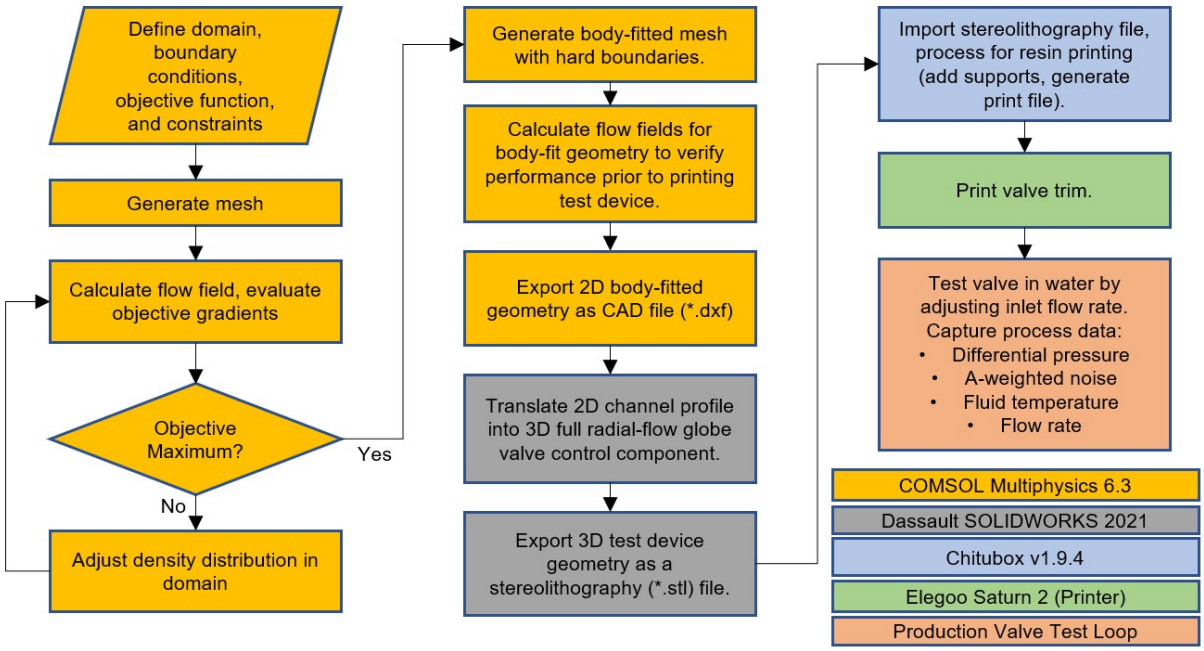


Figure 2. High-level development flow chart.

2.1. Valve Performance Equations

Cavitation potential is evaluated in control valves using an IEC standardized [20] definition of differential pressure ratio x_F as defined by:

$$x_F = \frac{p_1 - p_2}{p_1 - p_V} \tag{1}$$

where the absolute upstream static pressure, downstream static pressure, and fluid vapor pressure are given (generally in kPa) by p_1, p_2, and p_V, respectively. The upstream static pressure is required to be measured at the interior pipe wall, two nominal pipe diameters upstream the control valve and the downstream static pressure is measured six nominal pipe diameters downstream of the control valve. Increasing x_F reflects an increase in the potential of the device to cavitate. The point at which cavitation is acoustically detected is defined as the characteristic pressure ratio x_{Fz}.

At differential pressure ratio values greater than unity, the fluid within the domain of the control valve is no longer cavitating, but is rather flashing, as the vapor phase is maintained and the fluid no longer returns to a liquid state. Generally, without mitigation methods such as cavitation suppression mechanisms or material-based interventions, a control valve will begin to suffer damage at differential pressure ratios $x_F > 0.55$, while a highly staged valve trim may allow x_F greater than 0.99, i.e., devices that are better at

suppressing cavitation will have a higher measured value of x_{Fz}. As a corollary, such devices are generally much more resistant to cavitation damage, since cavitation occurs at geometric features with dramatically lower local static pressures.

Non-dimensional control valve flow capacity is measured and evaluated using the test procedures and equations described in the IEC standard 60534-2-3 [21]. For a fully turbulent flow, capacity (C_V) is calculated as:

$$C_V = \frac{Q}{N_1}\sqrt{\frac{\rho_1/\rho_0}{p_1 - p_2}} \tag{2}$$

where the volumetric flow rate is given by Q in (m^3/h), fluid density in (kg/m^3) at the inlet and at a reference state of 15 °C are given by ρ_1 and ρ_0, and a conversion constant N_1 of 0.0865 is used unify the traditional magnitude of C_V between metric and imperial units. For turbulent flows without phase change, measured C_V should not vary by more than 2.5% regardless of the pressure drop across the valve during testing.

2.2. Optimization Domain and Boundary Conditions

The primary control element of cavitation suppression control valves often consists of vertically stacked disks (repeated units) of defined capacity, whose summation makes a device with the desired full trim capacity. To prevent flow imbalances around the circumference of these radial flow devices, each of these disk repeat units are themselves formed by repetitions of wedge-shaped geometries. The analysis of these root-level repeated units form the basis for the prediction of the overall behavior of the system and are therefore the target for optimization.

A wedge-shaped flow domain (Figure 3a) was selected for optimization, with an outer radius of 3.175 cm (1.25 inch) and an inner radius of 1.589 cm (0.625 inch). These dimensions were chosen to conform to the standard internal trim footprint of a Flowserve Mark One ANSI 2-inch Class 150 globe valve. The interior angle of the wedge repeat unit was chosen to be 15°, which by observation is in the range of inlet distributions across this type of device (24 inlets distributed around the circumference). Too small of a wedge greatly restricts the passage size and the ability of the flow to travel in a circumferential direction; too large of a range and circumferential flow uniformity may be impacted. A parameterized study of the effect of this choice was not investigated, as in practice practical considerations drive the distribution in the range of 8 to 40 inlets; generally, a balance between passage size and channel height keeps repeat unit counts in the range of 12–30 to maintain the ability to pass particulate while also maintaining a smooth flow curve as each repeat unit is engaged. The choice of 24 repeat units therefore demonstrated the utility of the method with a domain choice within industry common practice. In the flow model, an inlet length of 0.825 cm and a flow exit length of 0.573 cm were incorporated to stabilize the inlet and outlet static pressure of the model. The determination of the inlet and outlet lengths is a function of the required capacity, as there will be nontrivial pressure distributions of the inlet and outlet lengths if there is insufficient flow area with respect to the domain's flow resistance; the effectiveness of these lengths as specified are discussed in Section 3.1.

To improve the ability of the optimization routine to develop multichannel geometry results and improve the uniformity of the flow in the optimization domain, a seeding routine was added as an initialization step. Radially spaced alternating islands of material (see Figure 3b) were placed in the domain so that optimization was initialized using a multichannel flow instead of a uniformly distributed single channel.

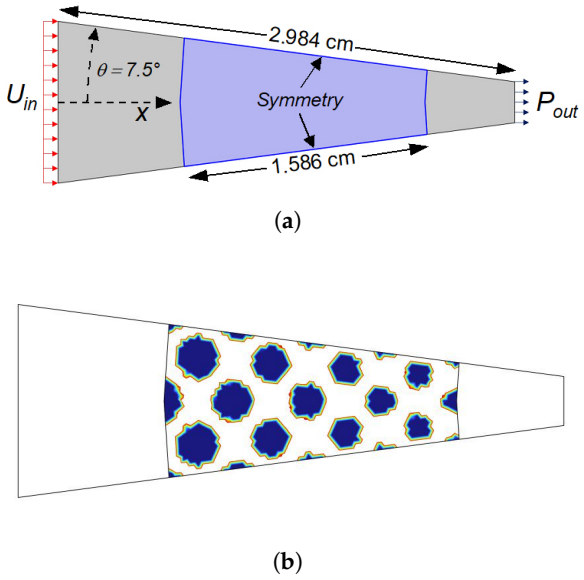


Figure 3. (**a**) Representation of optimization domain (blue) with inlet and outlet zones. (**b**) Design field distribution in domain at initialization.

Each model was initialized with a fixed inlet velocity determined by the respective target capacities (C_V): 0.672, 0.96, 0.96 (duplicate capacity target with an alternative objective function), and 1.248. A fixed pressure condition (0 Pa) was imposed on the outlet, and a symmetry condition was imposed on all remaining boundaries. Capacity is defined by the value C_V, the industry standard valve flow coefficient, a single scalar value that allows for the prediction of the flow rate in a fully turbulent flow given the properties of the operating fluid and the pressure drop across the system (see Section 2.1). The values for the target capacities were chosen to represent a typical repeat unit subsection flow rate for a staged anti-cavitation trim in this type and size of control valve. Incompressible water at 20 °C was the working fluid: density was 998.2 kg/m^3 and the dynamic viscosity was 1.00×10^{-3} Pa·s [22].

2.3. Cavitation Suppression Design Approach

The creation of cavitation suppression designs is rarely driven by a complete and direct simulation of multiphase flow phenomena, as such simulations are very computationally expensive [23,24] and prone to significant output variability [16,17]. Such simulations are generally limited to applications where the primary pressure drop of interest is expected to occur over a limited domain (e.g., a single hydrofoil). In addition to the computational expense, the implementation of a direct vaporization or local minimum pressure objective in a distributed large high pressure drop domain is largely counterproductive as an optimizer trying to keep local pressure above vapor pressure everywhere tends toward a single-stage geometry handling the full pressure drop in one location. This single location then has both a large static inlet and differential pressures, which drastically increases the energy and damage potential of the phenomena.

When the pressure drop is large and distributed, designs are often driven by pressure staging methods that suppress the extent and damage potential of cavitation by reducing static pressure in regions where cavitation is likely to occur. The pressure staging approach, designing the geometry to distribute the drop, is how the control valve industry has addressed cavitation suppression for decades. Since complete elimination of cavitation is often impractical due to footprint constraints and customer process conditions, reducing damage, vibration, and noise are the primary considerations of the cavitation-related design output. In this work, we use directional-change objective functions to generate

such static pressure reduction geometries in a full control-valve domain, in a manner that is capacity-specific. The objective function, by targeting directional change, drives the creation of geometries that increase velocity gradients and therefore total kinetic energy (TKE) production (Equation (7)). This energy extraction is a driver of kinetic energy leaving the mean flow, and it is reflected in the flow field as pressure drop. When the optimization maximizes directional change throughout the domain rather than at one location, it distributes TKE production spatially, generating multiple smaller pressure drops instead of a single large drop and therefore controls the nature, extent, and damage potential of fluid vaporization. As a further driver of pressure drop distribution, our implemented optimization routine includes a constraint on maximum velocity which directly limits changes in regional static pressure. Final flow test-based validations [20,25] were performed to confirm any assumptions about the design's characteristic cavitation initiation behavior, as x_{Fz} is not predicted by the model and requires physical validation.

2.4. Governing Equations

A detailed treatment of the governing flow and optimization philosophy used in this work is described in an earlier publication [19]. To minimize repetition, a concise replication of critical equations is repeated here, with increased detail where modifications and adjustments to equations and parameters have occurred.

The turbulent flows through the devices described in this work were simulated using a modified Reynolds-Averaged Navier–Stokes (RANS) model, Equations (3) and (4):

$$\rho(\mathbf{u}\cdot\nabla)\mathbf{u} + \nabla p - \nabla\cdot\left((\mu+\mu_T)\left(\nabla\mathbf{u}+(\nabla\mathbf{u})^T\right)\right) + \alpha\mathbf{u} = 0 \tag{3}$$

$$\nabla\cdot\mathbf{u} = 0 \tag{4}$$

The fluid's mean velocity, fluid pressure, mass density, dynamic viscosity, turbulent viscosity and Brinkman penalty factor are given by $\mathbf{u}$, p, ρ, μ, μ_T, and α, respectively. The final term in Equation (3), which includes the Brinkman penalty factor, was used to make the flow model compatible with density-based topology optimization and is described further in Section 2.5.

Turbulence closure was provided by the two-equation $k-\varepsilon$ model (5) and (6) and the associated equations for turbulent kinetic energy production (7) and turbulent viscosity (8):

$$\rho\frac{\partial k}{\partial t} + \rho\mathbf{u}\cdot\nabla k - \nabla\cdot\left(\left(\mu+\frac{\mu_T}{\sigma_k}\right)\nabla k\right) - P_k + \rho\varepsilon = 0 \tag{5}$$

$$\rho\frac{\partial \varepsilon}{\partial t} + \rho\mathbf{u}\cdot\nabla\varepsilon - \nabla\cdot\left(\left(\mu+\frac{\mu_T}{\sigma_\varepsilon}\right)\nabla\varepsilon\right) - C_{\varepsilon1}\frac{\varepsilon}{k}P_k + C_{\varepsilon2}\rho\frac{\varepsilon^2}{k} + \alpha_\varepsilon(\varepsilon-\varepsilon_w) = 0 \tag{6}$$

$$P_k = \mu_T\left(\nabla\mathbf{u} : \left(\nabla\mathbf{u}+(\nabla\mathbf{u})^T\right)\right) \tag{7}$$

$$\mu_T = \rho C_\mu\frac{k^2}{\varepsilon} \tag{8}$$

The parameters of the turbulence model are shown in Table 1. The last term of Equation (6) was introduced to facilitate topology optimization, which is explained further in the following section.

Table 1. k-ε Turbulence Model Parameters.

C_μ	$C_{\varepsilon1}$	$C_{\varepsilon2}$	σ_k	σ_ε
0.09	1.44	1.92	1.0	1.3

Linear stabilized finite elements were used to discretize the governing equations within COMSOL v.6.3 [26]. A segregated solver and pseudo-transient continuation (default settings) were used to solve the coupled nonlinear system of equations. The direct solver Pardiso was used to solve linear systems.

2.5. Topology Optimization Equations for Flow and Turbulence

The gradient-based optimization algorithm uses a design field that varies from 0 to 1, $\gamma \in [0;1]$, where 0 and 1 represent solid and fluid regions, respectively. This field is allowed to vary and is connected to the governing equations through interpolation functions. The first (Equation (9)) is the Brinkman penalty introduced as the last term of Equation (3) which models the flow resistance in the solid part of the domain by setting the Brinkman penalty to a large number. As material is added by the optimization routine, flow resistance proportional to this penalty takes place at the material location and therefore pressure and velocity behavior are modified: the modifications are evaluated against the objective criteria and subsequent material addition or subtraction occurs.

$$\alpha(\gamma) = \alpha_{\min} + (\alpha_{\max} - \alpha_{\min})\frac{q(1-\gamma)}{(q+\gamma)} \tag{9}$$

$$\alpha_{\min} = \frac{10\mu}{{h_{ch}}^2} \tag{10}$$

$$\alpha_{\max} = 10^5 \cdot \alpha_{\min} \tag{11}$$

This proportional resistance factor α hits a maximum value ($\alpha_{\max}$) when $\gamma = 0$, that is, the design fields dictate a solid region. Since the simulation of the flows in the domain must be numerically tractable, $\alpha_{\max}$ cannot be infinite, even though this would drive the calculated velocities flow in the "solid" regions to zero and ensure no-slip conditions at the channel boundaries. Instead, this value is set to a very high value to heavily penalize the flow in the solid regions. Since this work considers the channel depth to be finite, an approximation of $\alpha_{\min} = 6947.9\ \text{Pa} \cdot \text{s/m}^2$ is made using the out-of-plane viscous resistance equation seen in (10) [7,8,27] where the distance of the plates is given by $h_{ch} = 0.12$ [cm]. The parameter q is an interpolation value used to push the design field (γ) towards the bounds of 0 and 1 and penalize intermediate values. In this study, it was set to a value of 1000.

As described in [19], adjustments were made to the $k-\varepsilon$ turbulence model as implemented in COMSOL turbulence equations [26,28] to include parts of the wall functions:

$$\varepsilon_w = \rho\frac{C_\mu k^2}{\kappa_v \delta_w^+ \mu} \tag{12}$$

$$\delta_w^+ = \max\left(11.06, \frac{\rho {C_\mu}^{1/4}\sqrt{k}h_e}{2\mu}\right) \tag{13}$$

$$\alpha_\varepsilon(\gamma) = \alpha_{\max}\frac{q(1-\gamma)}{(q+\gamma)} \tag{14}$$

The wall boundary condition for ε as seen in Equation (12) has a von Kármen (κ_v) constant of 0.41 and has the wall lift-off as described in Equation (13), where h_e is the COMSOL effective element size. The boundary condition for the k variable is a zero normal gradient condition and has been observed to not be as important to the topology optimization model, and so no penalty term was applied to the turbulent kinetic energy variable. At the boundaries, we relied on the heavy penalty term in Equation (3) to approximate a no-slip condition, and the penalty term α_ε (14) was applied to the dissipation

variable ε in the turbulence Equation (6) to drive it to the non-zero value ε_w. α_{max} and q are the same values as used in Equation (9).

2.6. Valve Trim Flow Channel Objective Functions

In order to control the drop in pressure across the control valve trim, two directional change objective functions were selected: an x-direction formulation (maximize $\frac{\partial u}{\partial x}$) similar to that demonstrated in the single channel device discussed in [19] and a new radial formulation (maximize $\frac{\partial v_\theta}{\partial r}$):

$$\phi_1(\mathbf{u}, \gamma) = \int_\Omega \left(\frac{\partial u}{\partial x}\right)^2 d\mathbf{r} \tag{15}$$

$$\phi_2(\mathbf{u}, \mathbf{v}, \gamma) = \int_\Omega \left(\frac{\partial v_\theta}{\partial r}\right)^2 d\mathbf{r} \tag{16}$$

where the u is the velocity in the x-direction and the tangential velocity ($v_\theta = r\dot{\theta}$) was implemented in cartesian coordinates as $v_\theta = \frac{xv - yu}{\sqrt{x^2+y^2}}$. These objectives were deemed good candidates for initial valve trim designs as they should create designs similar in geometric composition to current state of the art tortuous path designs (e.g., Figure 1b) which have a demonstrated ability to dissipate flow energy and reduce the incidence and damage potential of cavitating flow. For the ϕ_1 objective, the primary inlet-to-outlet axis of flow was along the x-axis. Similarly, the ϕ_2 objective defines the primary axis of flow to be in the radial direction, from the outer diameter to the inner and the primary velocity to be perpendicular to the direction of change (prioritizing velocity change conceptually opposite that of the ϕ_1 objective. The objectives therefore maximized the amount of off-axis flow within the bounds of the optimization problem constraints.

The optimization routine maximizes these objectives under the following constraints: a fixed boundary-to-boundary pressure drop, a maximum in-domain velocity, and a maximum fluid volume. Formally, this optimization problem is defined by Equation (17), where $p^* = 10$ kPa is the maximum allowable pressure drop, $V^* = 0.4$ is the maximum fluid volume fraction, and $U^* = 2.5$ m/s is the p-mean maximum allowable local velocity magnitude:

$$\begin{aligned} \underset{\gamma \in L^2(\Omega)}{\text{maximize}} \quad & \phi \\ \text{subject to:} \quad & \Delta p_{\text{system}} && \leq p^* \\ & V && \leq V^* \\ & U_{\max} && \leq U^* \\ & 0 \leq \gamma(\mathbf{r}) \leq 1 && \text{for all } \mathbf{r} \in \Omega \end{aligned} \tag{17}$$

where the constraints are defined as:

$$\Delta p_{\text{system}} = \frac{1}{|\Gamma_{\text{in}}|} \int_{\Gamma_{\text{in}}} p \, ds - \frac{1}{|\Gamma_{\text{out}}|} \int_{\Gamma_{\text{out}}} p \, ds \tag{18}$$

$$V = \frac{1}{|\Omega_d|} \int_{\Omega_d} \gamma \, d\mathbf{r} \tag{19}$$

$$U_{\max} = \left(\frac{1}{|\Omega_d|} \int_{\Omega_d} \left(\sqrt{u^2 + v^2} \right)^P d\mathbf{r} \right)^{\frac{1}{P}} \tag{20}$$

The system pressure drop was evaluated as shown in Equation (18), with Γ_{in} as the inlet boundary and Γ_{out} the outlet boundary. The relative fluid volume fraction function was calculated by (19), and Equation (20) was the approximation of the max velocity in the domain using a continuous p-mean where $P = 20$ is the p-mean factor (a large enough

value that the power mean approaches the magnitude of the maximum velocities on the domain). Ω_d is the design domain.

2.7. COMSOL Optimization Module Setup

COMSOL was used to implement the optimization equations using its built-in "Optimization Module" [29]. Optimization variables are the nodal design field variables of the linear finite elements used in the COMSOL discretization, and a Helmholtz PDE filter [30] with $R_f = 0.058$ cm was used for regularization. A Heaviside projection was used to reduce the design variable transition at the fluid-solid interface. The projection threshold was 0.5, and the projection parameter was 14 (unramped). COMSOL's symbolic differentiation [29] was used to drive the adjoint computation of sensitivities; the design was updated using the Globally Convergent Method of Moving Asymptotes (GCMMA) [31] with a maximum inner iteration of 2. A design variable (total, not nodal) move limit of 2% was applied to allow the flow solver to converge between design updates.

2.8. Post-Processing

As the optimization routine depends on intermediate permeability, upon completion of the optimization process the fluid–solid interface was forced to a binary state through the use of a filter. The design variable cutoff value, which ranges from 0 to 1, is determined by simulating the hard-boundary flow field (see Section 3.1) and matching the calculated domain pressure drop with the pressure drop objective. As the optimization routine was robust, the domain pressure drop target was achieved for all target capacities with filter values in the range of 0.6 to 0.75. For context, a poorly executed optimization has excessive intermediate density values in the channels and no filter cutoff value produces a hard-boundary design with the target pressure drop. The hard-boundary flow simulation uses the same flow model and settings as the optimization routine. As there are no intermediate values of the design variable, the out-of-plane compensation value is constant at α_{min}.

2.9. Device Fabrication

After the optimization process was complete, the generated 2D geometries were extruded to a target channel depth (0.12 cm), mirrored, radially patterned, and incorporated into a 3D disk repeat unit. These four designs, three of which were generated with the ϕ_1 objective with target capacities of 0.672, 0.96, and 1.248, and one of which was generated with the ϕ_2 objective (target capacity 0.96), can be seen in Figure 4.

Next, structures were generated to support and seal the repeat units into the globe valve, which acts as the inlet and outlet manifolds. The completed valve trim model, seen in Figure 5a, had an outer diameter of 6.604 cm, a minimum inner diameter of 3.18 cm, and a length of 7.607 cm. The completed digital model was then converted into a Standard Tessellation Language (.stl) file and fabricated using an Elegoo Saturn 2 8K MSLA printer which uses a high-resolution (7680 × 4320 pixel, 305.9 mm × 273 mm, 28.5 µm XY pixel size) screen to mask and expose the resin to ultraviolet (UV) light, creating a solid with a 30 µm layer resolution (Figure 5b). The resin of choice was Siraya Tech's "Blu Nylon Black", which has a yield strength of 47 MPa and a modulus of 1750 MPa, which is far in excess of what is needed at our test pressure of 0.7 MPa (no leakage or deformation was observed during testing). A ten-minute post print curing cycle was completed using a rotating 405 nm UV cure chamber. Print settings are shown in Table 2.

Resin devices were chosen vs. printed steel as the relevant requirement for validation and device comparison is a rigid channel with no-slip boundaries and correct geometry, as well as rapid fabrication and low cost. Once a compatible objective formulation method is evaluated and selected, final capacity tuning can occur using surface roughness corrections in the final 3D simulation for the material and fabrication method of choice. The material-

by-material differences in x_{FZ}, which may be significant in a single stage device, are significantly lower in a multistage device as the proportion of pressure drop handled by the final cavitating feature is small; however, these may also be quantified by material-specific testing. Examples of roughness and material dependent performance and simulation are widespread (e.g., [32–34]) but are not a focus of this work.

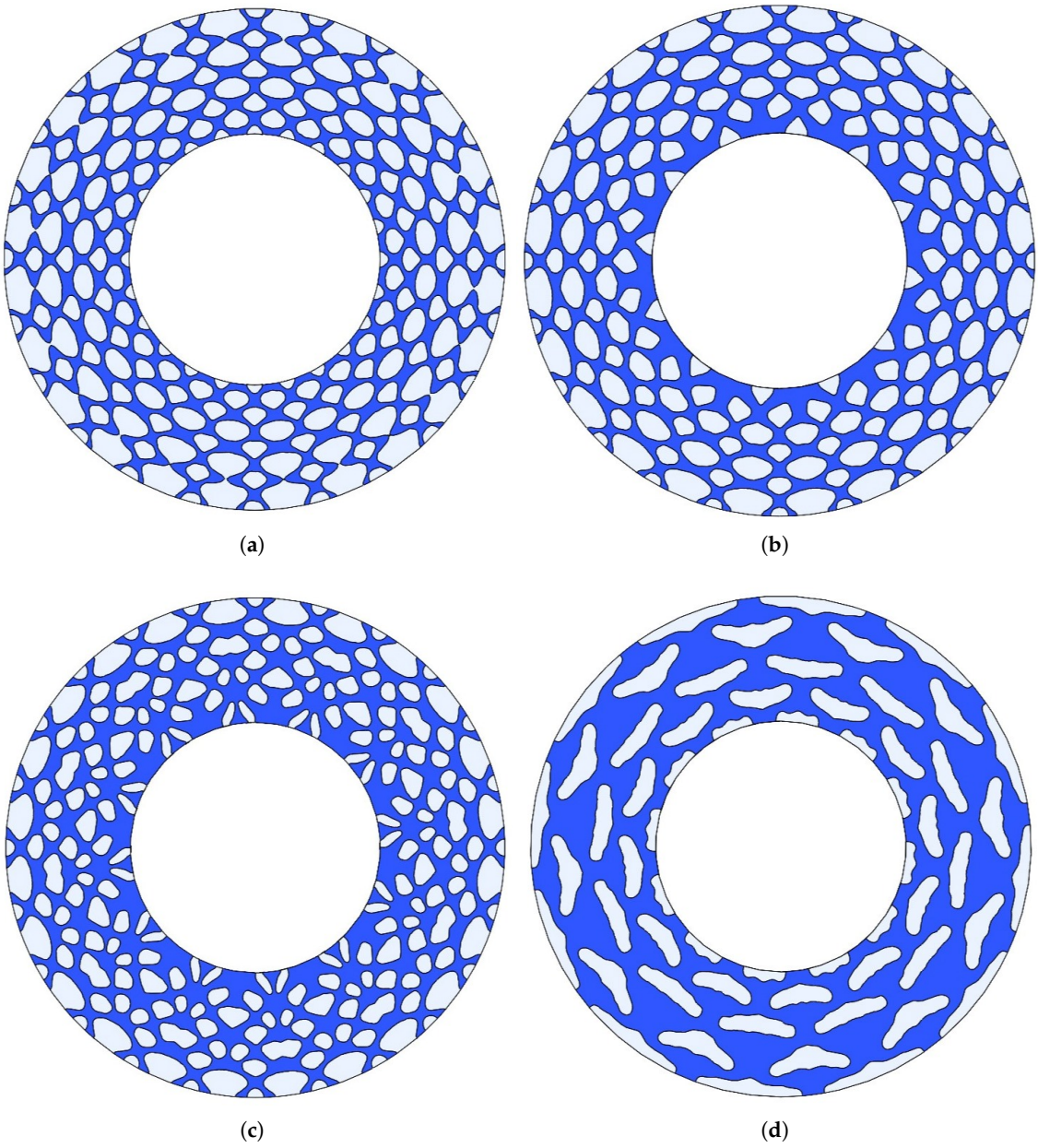
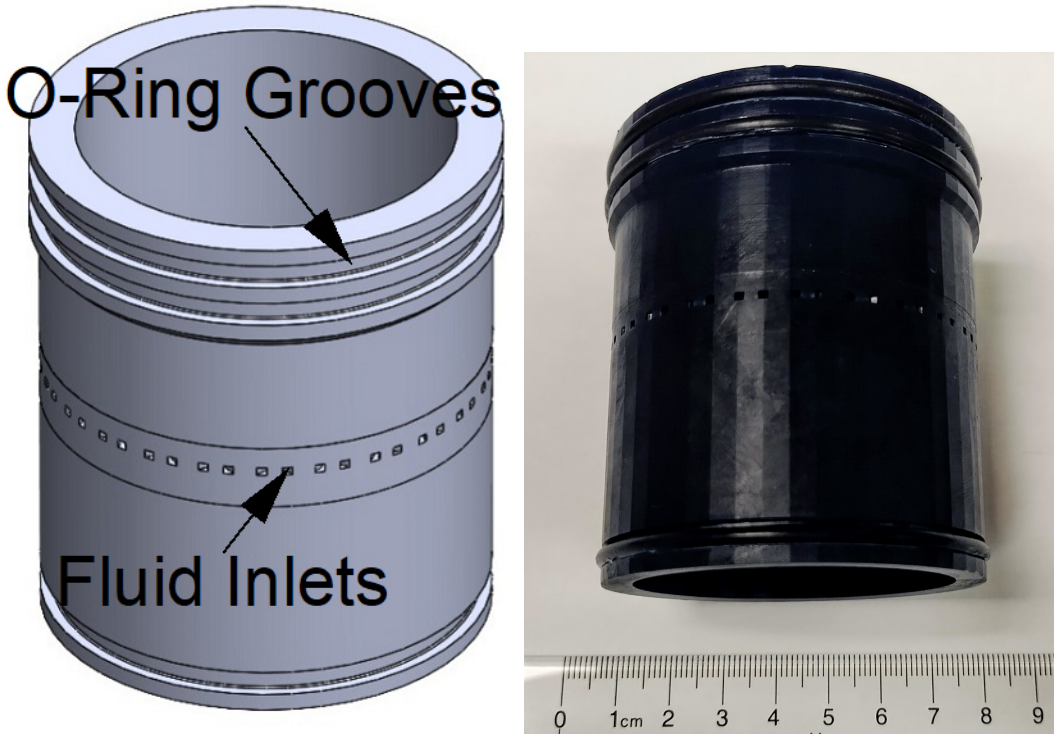


Figure 4. Channel layer geometry for tested devices. Channel depth is 0.12 cm. (**a**) Maximized ϕ_1 device, 0.672 nominal capacity. (**b**) Maximized ϕ_1 device, 0.96 nominal capacity. (**c**) Maximized ϕ_1 device, 1.248 nominal capacity. (**d**) Maximized ϕ_2 device, 0.96 nominal capacity.

Table 2. MLSA Print Settings.

Room and Resin Temp (°C)	Layer Height (μm)	Layer Exposure (s)	Initial Layers	Initial Layer Exposure (s)
26.5	30	3	5	15



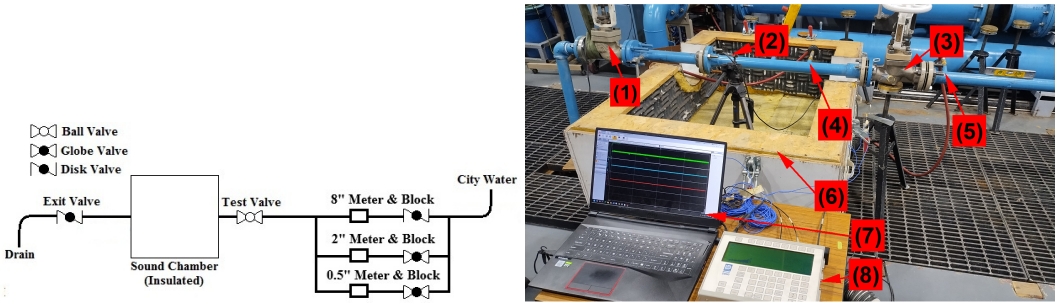
(**a**) (**b**)

Figure 5. Structure and example of printed test device. (**a**) Three-dimensional view of test device. (**b**) Printed test device.

2.10. Experimental Setup

An ANSI Class 150 Flowserve Mark One globe-style control valve was used to evaluate the capacity and cavitation suppression performance of the four TO-generated control valve trims. The valve was installed in a water test line (2-inch) configured in accordance with IEC capacity testing [21] and acoustic testing [20] guidelines. As per standard, pressure tap locations were located two nominal pipe diameters (10.16 cm/4 inches) upstream of the test valve inlet and six nominal pipe diameters (30.48 cm/12 inches) downstream of the test valve outlet. Static pressure was measured upstream as p_1 and differentially across the upstream and downstream pressure taps as Δp using Rosemount 3050S1 inline pressure transmitters with 0.5% full-scale accuracy and 1034.2 kPa absolute (150 PSIA), 1034.2 kPa differential, and 206.8 kPa differential (30 PSID) ranges, respectively. An instrument change occurs from the low-range to the high-range differential pressure sensor when Δp exceeds 172.4 kPa (25 PSID). Flow was measured using a 6.36 m^3/h (28 gallons per minute) $\frac{1}{2}$-inch Rosemount 8712 magnetic flow meter with a 0.15% full-scale accuracy, and temperature was measured at the inlet using an 100-ohm RTD with Class A accuracy ($\pm$0.19 °C at 20 °C). Another 2-inch throttling valve was located 1.3 m (51.4 inches) downstream of the valve and was used to control the pressure drop ratio in the test sample. Figure 6a shows a simplified representation of the flow configuration. The pipe directly downstream of the test control valve passed through the center of a sound isolation chamber and was fitted with sound-absorbing insulation on all surfaces. To acoustically detect cavitation, a Larson–Davis model 2559 microphone with an attached 900B preamplifier was placed 37.5 cm from the downstream pipe wall, directly facing the pipe centerline. This distance was reduced from the noise testing standard's 1 m guideline due to space constraints, which increased the sensitivity of the cavitation detection but introduced a 3 dBA bias in the 1 m industrial noise measurement (which is not relevant to this work). A-weighting of

the acoustic signal was performed using a Larson–Davis 2900 sound level meter; this test setup can be seen in Figure 6b.



(**a**) (**b**)

Figure 6. Structure and example of printed test device. (**a**) Simplified layout of test pipe. (**b**) Acoustic testing setup. Acoustic testing components are as follows: (1) Throttling valve. (2) Microphone. (3) Test valve. (4) Downstream pressure tap. (5) Upstream pressure tap. (6) Sound chamber (open). (7) Data acquisition. (8) Sound level meter.

The combined standard uncertainty of the calculated capacity (C_V) and characteristic pressure drop ratio (x_{Fz}) for each test are shown with the test results in Section 3.4, and were calculated using Equation (21) (see [35]) where u_{Xi} are the combined standard uncertainties in the measured process variables X_i. In the current work, these include the process variables P_1, P_2, Q, and T, and the property variables ρ and P_V.

$$u_r^2 = \left(\frac{\partial r}{\partial X_1}\right)^2 u_{X_1}^2 + \left(\frac{\partial r}{\partial X_2}\right)^2 u_{X_2}^2 + \cdots + \left(\frac{\partial r}{\partial X_J}\right)^2 u_{X_J}^2 \quad (21)$$

During each test, line pressure (670 kPa) city water was introduced to the test loop and the test system was purged of ambient air over a five minute cycle. No de-aeration or measurements of local concentration of dissolved solids were performed (the standard does not require such mitigation), which may slightly influence the measured values of x_{Fz} when changing between regional test facilities. Initially, the downstream throttling valve was closed and the differential pressure across the valve was zero. The downstream throttling valve was then opened in small increments to increase the pressure drop ratio across the valve by $\Delta x_F = 0.025$, culminating in a system maximum available (limited by water supply) pressure drop ratio of $x_F = 0.86$. At each targeted process condition, the flow rate, pressures, temperature, and A-weighted noise were recorded. As these pressure drops are far in excess of the optimization routine's 10 kPa differential pressure, it is important to recognize that the target parameters are the device capacity (the direct target of the simulation, which is verifiable at any fully turbulent flow condition) and cavitation performance, which is not an output of the flow simulations. As such, target capacity (C_V) is the primary metric to determine the utility and accuracy of the TO method for the generation of fit-for-purpose valve trims.

3. Results

3.1. Optimized Topology Flow Field

Cavitation severity is a function of both the static pressure just upstream of the pressure drop and the magnitude of the pressure drop driving fluid vaporization. It therefore follows that a driving goal for a cavitation suppression device is to radially "front load" pressure drop, i.e., take large pressure drops (limited by velocity constraints) nearer the geometric inlet of the device and as far as possible fluid at or near vapor pressure. To better understand the behavior of the generated valve trim geometries, each optimized domain had a mesh

fitted to the optimized domain using a design field threshold and were subsequently analyzed using COMSOL.

The resultant pressure fields showed that for the ϕ_1 objective the large majority (80%) of the static pressure reduction, as seen in Figure 7a–c, had occurred by 50% of the radial distance through the optimized domain (0.75 cm from optimized domain inlet). Areas of increased velocity driven by these pressure reductions, seen in Figure 8a–c, are likewise concentrated further from device outlets. As the bulk of the pressure drop in these three devices was occurring with significant staging remaining, the magnitude of the remaining pressure gradients were decreased which in turn reduced the severity of cavitation when the fluid was near the vapor pressure. As seen in Figure 7d, the converse was true for the ϕ_2 objective device which was still showing pressure values 80% of inlet at the same radial location as well as large velocity spike (90% of domain maximum, see Figure 8d) at the final inlet. A comparison of the maximum velocities vs. radial position may be seen in Figure 9. Both of these factors contributed to reduced ϕ_2 device cavitation suppression performance vs. the equivalent ϕ_1 device. The simulated maximum velocity and minimum pressure of each device are shown in Table 3.

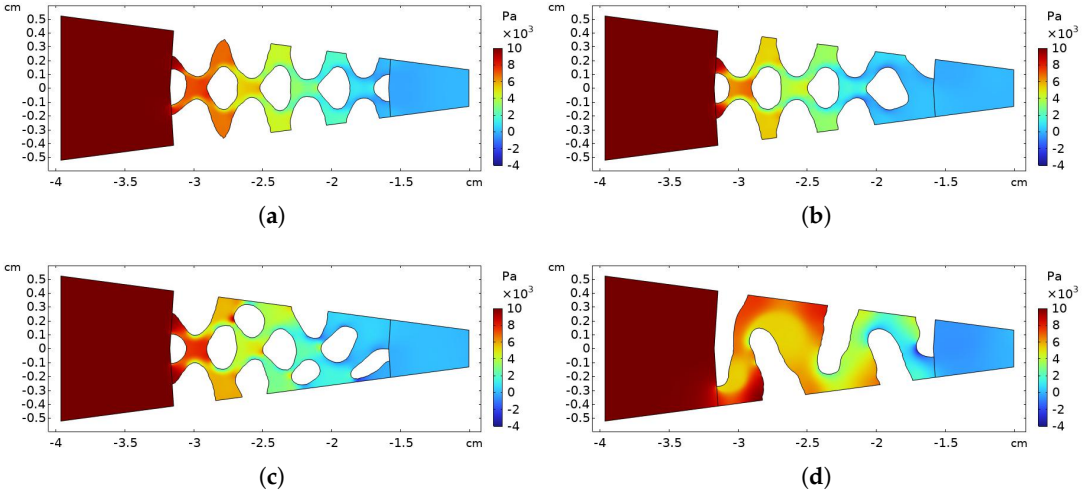


Figure 7. Generated geometry repeat unit static pressure fields. (**a**) Maximized ϕ_1 device, 0.672 C_V. (**b**) Maximized ϕ_1 device, 0.96 C_V. (**c**) Maximized ϕ_1 device, 1.248 C_V. (**d**) Maximized ϕ_2 device, 0.96 C_V.

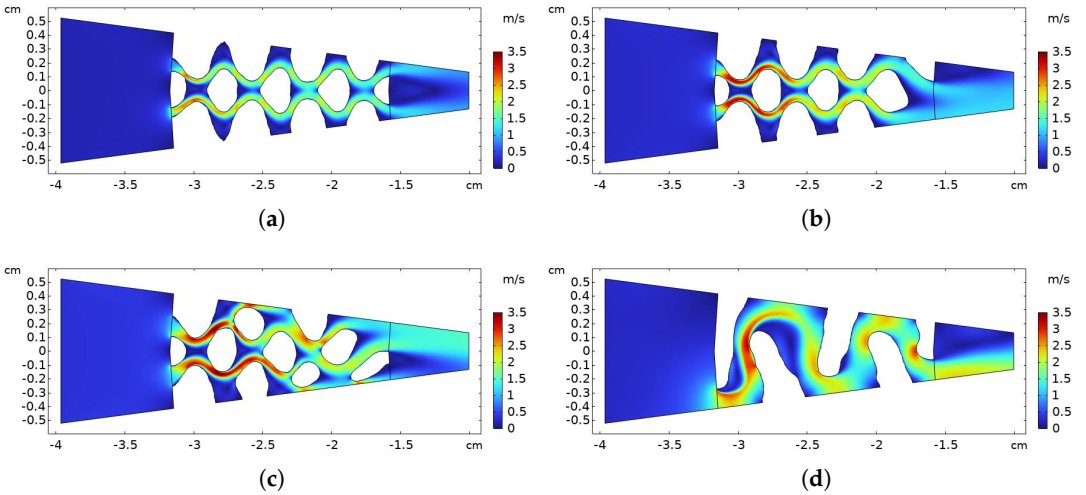


Figure 8. Generated geometry repeat unit velocity fields. (**a**) Maximized ϕ_1 device, 0.672 C_V. (**b**) Maximized ϕ_1 device, 0.96 C_V. (**c**) Maximized ϕ_1 device, 1.248 C_V. (**d**) Maximized ϕ_2 device, 0.96 C_V.

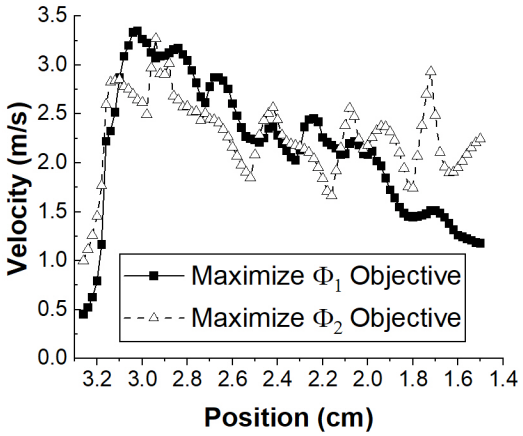


Figure 9. Maximum channel velocities per radial position for equivilent nominal capacity ($C_V = 0.96$) ϕ_1 and ϕ_2 devices.

Table 3. Element Maximum Velocity, Minimum Pressure, and Non-Uniform Hydraulic Diameter from Hard Boundary Simulations at $\Delta P = 10$ kPa per Constraint.

Objective	Target C_V	V_{max} (m/s)	P_{min} (Pa)	D_H (cm)
ϕ_1	0.672	2.876	−1125.38	0.101
ϕ_1	0.96	3.365	−1357.98	0.119
ϕ_1	1.248	3.535	−4162.35	0.123
ϕ_2	0.96	3.308	−3886.84	0.162

Examining each generated geometry, the nature of the driving objectives can be clearly seen (Figure 4). The ϕ_1 devices showed continuous flow velocity variation in x by a prioritization of 45° channels with non-zero x-velocity and a maximization of the number of directional changes. The ϕ_2 objective successfully increased the tangential velocities and subsequently the magnitude of the velocity changes as radial channels were repeatedly reversed.

After comparing the performance of the ϕ_1 devices in different capacities, it was clear that as target capacity increased localized velocity spikes were occurring further towards the radial center. The corollary of this effect was the encroachment of low-pressure regions radially upstream, as well as increases in the number and magnitude of such regions in the optimized domain. To more clearly illustrate the result, pressure plots scaled to highlight minimum pressures are shown in Figure 10. The trend of reducing cavitation suppression as capacity increases was expected, as less interference with flow can be tolerated in a given fixed geometric domain as required throughput increases. One means of quantifying this effect is to examine the non-uniform hydraulic diameter of each device, which is defined as a multiple of the ratio of wetted channel volume to channel surface area:

$$D_H = \frac{4V}{S} \tag{22}$$

The calculated values for D_H are shown in Table 3. Intuitively, as the hydraulic diameter decreases there is more flow resistance (more surface area) per unit of channel volume. This has the effect of decreasing capacity, or for constant capacity driving an increased reduction in flow energy. The results of the cavitation detection testing (see Section 3.4) supported this assumption, showing monotonically decreasing values of x_{F_z} with increasing values of D_H.

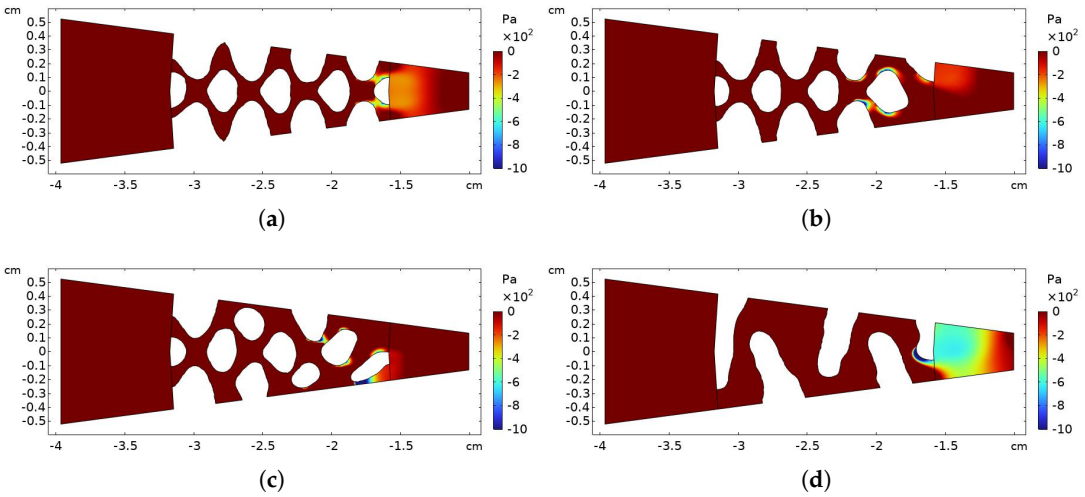


Figure 10. Static pressure fields, scaled for low pressure contrast. (**a**) Maximized ϕ_1 device, 0.672 C_V. (**b**) Maximized ϕ_1 device, 0.96 C_V. (**c**) Maximized ϕ_1 device, 1.248 C_V. (**d**) Maximized ϕ_2 device, 0.96 C_V.

Contrasting the reduced performance of the ϕ_2 objective trim with respect to its specific capacity pair (Figure 8d vs. Figure 8b), we saw there were clear distinctions in performance driven by objective selection even though capacities were equivalent. The ϕ_2 objective drove the creation of aggressive full 180° flow direction changes, which tended to drive larger low pressure regions even near the outlet. The trim generated using this objective also had the highest calculated value of D_H.

An indication of the ability of these designs to suppress damaging cavitation was the location of the pressure minima in conjunction with surrounding static pressure in the channel. In the design seen in Figure 7a, the first subzero (gauge) pressure minima occurred when the static pressure of the surrounding channel was close to the outlet pressure (0 Pa). In contrast, as seen in Figure 7c,d, the static pressures of the surrounding channel were approximately 1500 Pa and 1000 Pa, respectively. To provide better resolution as to the location of these low pressure minima, the pressure fields scaled for low pressure contrast may be seen in Figure 10. As higher channel pressures in the domain where there are low pressure excursions increase the intensity and the damage potential of the cavitation, the first example listed (ϕ_1 device, 0.672 C_V) was deemed to be the most effective. This prediction was consistent with the results of the acoustic testing as presented in Section 3.4.

3.2. Optimization Parameter Sensitivity Analysis

To assess the robustness of the optimization framework, we conducted a sensitivity study on the ϕ_1 device (target C_V = 0.96) by varying key optimization parameters. Table 4 presents the results given variations in the Helmholz filter radius R_f, the Heaviside projection parameter β, and the Brinkman interpolation value q. Note that while the target parameter variation was ±25%, the maximum positive variation for β was 14% and the maximum negative variation for q was 15%, as the optimization became unstable and failed to converge when these variables were driven further. All tabulated runs converged and produced the desired capacity in the 2D hard boundary simulation, with required cutoff filter values remaining within 15% of baseline (see Table 4, "Filter Value at Target C_V"). Baseline performance was the most optimal, with the exception of a minor improvement using the β-configuration which had a 5% improvement in the minimum element pressure and a 1.7% reduction in the maximum element velocity. Changes in channel structure can be seen in Figure 11 for each of the variations in optimization parameters. These changes are concentrated at the outlet, where sensitivity to the optimization function is lower due to

reduced local static pressure. Given these results, the baseline settings for the optimization functions were considered sufficiently stable for the current scope of work without further extensive parameter tuning.

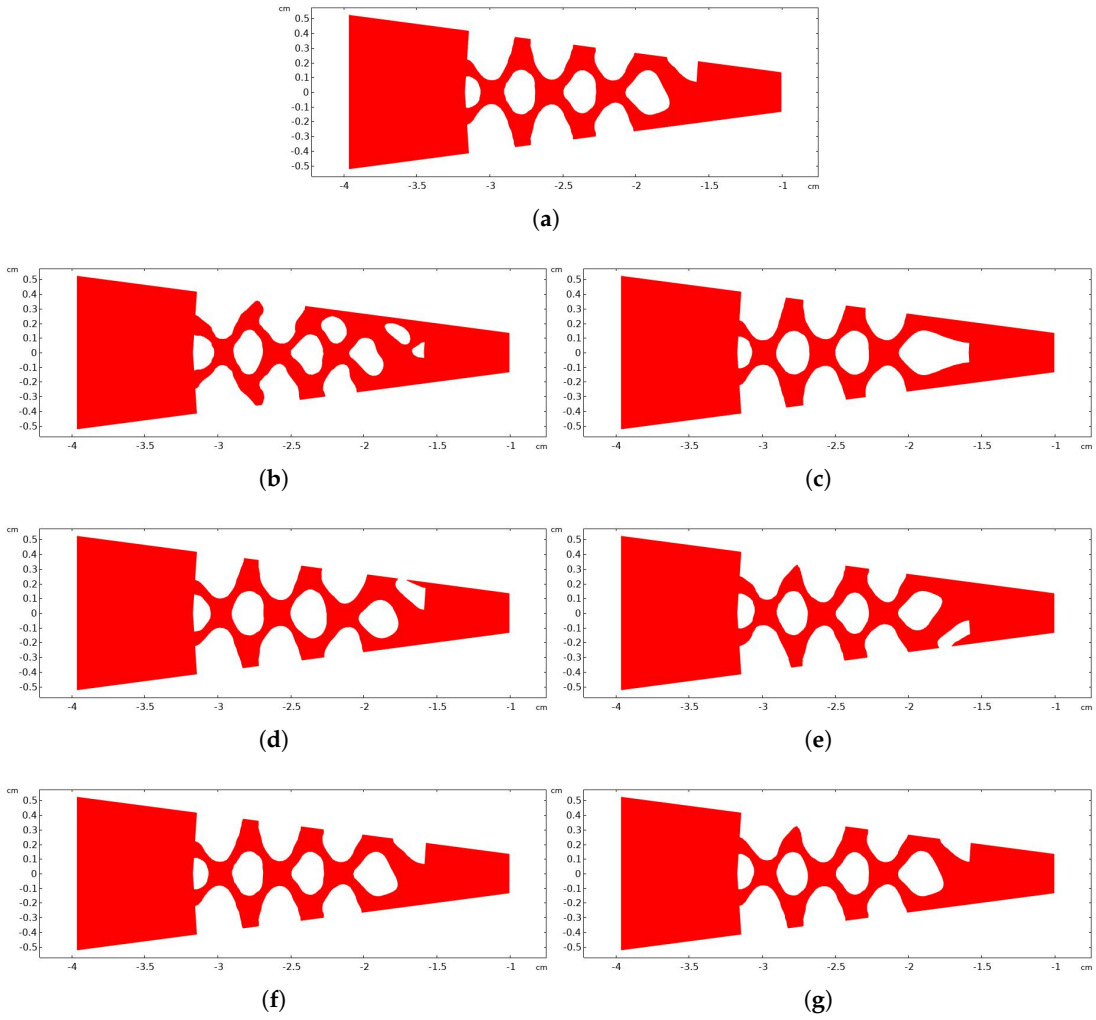


Figure 11. Variations in optimization geometry output for ϕ_1 objective over variations of optimization parameters. (**a**) Baseline variant. (**b**) R_f- variant. (**c**) R_f+ variant. (**d**) β- variant. (**e**) β+ variant. (**f**) q- variant. (**g**) q+ variant.

Table 4. Optimization Parameter-Driven Calculation Variations.

Description	R_f (cm)	β	q	Filter Value at Target Cv	Min Element Pressure (Pa)	Max Element Velocity (m/s)
Baseline	0.058	14.0	1000	0.745	−1338.7	3.36
R_f-	0.043	14.0	1000	0.758	−1891.1	3.64
R_f+	0.072	14.0	1000	0.630	−1800.5	3.60
$\beta-$	0.058	10.5	1000	0.678	−1271.4	3.30
$\beta+$	0.058	16.0	1000	0.771	−1334.2	3.53
$q-$	0.058	14.0	850	0.773	−1538.7	3.39
$q+$	0.058	14.0	1250	0.715	−2004.5	3.55

3.3. Mesh Convergence Analysis

For the simulation results reported in Section 3.1, a mesh convergence analysis was performed to determine the sensitivity of maximum element velocity, minimum element pressure, and system pressure drop (and therefore C_V) to mesh size. The minimum mesh

element size was refined by 50% (sequentially, as seen in Table 5) and the hard-boundary simulation was re-run with a solution-based termination criteria of 2×10^{-5}. Output variations were as seen in Table 6. Changes in capacity (C_V), the primary parameter of interest, were a maximum of 0.53% for all simulations when moving from the reference to fine mesh; only the minimum element pressure showed significant mesh sensitivity (with a maximum of 19% in the ϕ_2 device simulation). The reference mesh was selected as sufficiently refined to provide a comparison with experimental capacity results.

Table 5. Mesh Refinement Settings.

Description	Max Element Size (cm)	Min Element Size (cm)	Max Element Growth Rate	Curvature Factor
Coarse	0.07	0.00313	1.2	0.4
Reference	0.047	0.00209	1.15	0.3
Fine	0.0365	0.00104	1.13	0.3

Table 6. Refinement-Driven Calculation Variations, Relative Change to Reference Mesh.

Geometry	Mesh Setting	C_V (%)	Boundary Pressure Δp (%)	Min Element Pressure (%)	Max Element Velocity (%)
ϕ_1, 0.672 Target C_V	Coarse	−0.29	0.58	−1.93	−0.33
	Fine	−0.77	−1.53	1.13	0.19
ϕ_1, 0.96 Target C_V	Coarse	−0.08	0.16	0.12	−0.15
	Fine	0.52	−1.04	1.59	−0.16
ϕ_1, 1.248 Target C_V	Coarse	−0.58	1.17	−7.19	0.78
	Fine	0.53	−1.05	0.94	−0.15
ϕ_2, 0.96 Target C_V	Coarse	−0.44	0.89	−0.06	−0.26
	Fine	0.16	−0.32	19.47	0.19

3.4. Flow and Noise Performance of Tested Devices

The capacity testing results of the control valve with printed trims are shown in Table 7. The expectation for a commercial trim was that the delivered capacity would be no more than ±10% nominal. The trims generated through the two-dimensional optimization and simulation methods described in this work ranged in accuracy, when compared to the in-valve water test results, from 13.7% below target to 4.8% above target with an average of 6% below target. Replacing the 2D hard-boundary simulation with a refined mesh 3D hard-boundary simulation (see Section 3.5) using a steady-state $k-\epsilon$ turbulence model reduced the maximum simulation error to 7.8%. The range of error described above includes all variations in both the design, fabrication, and testing processes such as 2D simulation results driving a 3D-printed part, experimental uncertainty, and printing variations. Surface roughness was not input into the simulated flow model, as it is low (S_a of 6.7 to 8.5 µm) [36] for MSLA printed surfaces. In industrial service, these devices will be fabricated using established metal additive processes (e.g., selective laser melting or SLM) as has been adopted in the industry [37]. Each chosen material and printing process require its own process tuning to ensure dimensional accuracy and that compensations for the capacity impact of surface roughness are applied [32–34] and to establish cavitation performance damage thresholds.

The cavitation suppression performance of the valve components procedurally generated from the ϕ_1 objective (nominal capacities of 0.672, 0.96, and 1.248) and the ϕ_2 objective (nominal capacities of 0.96) can be seen in Figure 12a–d, respectively. As discussed in Section 3.1, the characteristic pressure drop ratio (x_{Fz}) at which cavitation is detected steadily decreased as the required capacity increased. For context, the lowest-performing

device (ϕ_2 objective, nominal capacity of 0.96) had an x_{Fz} value of 0.727 which is comparable to current moderately-staged devices in industrial use (a value of x_{Fz} of 0.5 is typical for a control valve without cavitation suppression features). The highest performing device (ϕ_1 objective, nominal capacity of 0.672) had very effective cavitation suppression performance, with an x_{Fz} value greater than 0.865 (considered highly staged). Restrictions on the ability of the test laboratory to reduce downstream pressure below 0.86 bar (absolute) prevented determining the full performance range of this device (Figure 12a). All values of x_{Fz} can be seen in Table 7 and are calculated from test results according to Equation (1).

Table 7. Experimental Results and Uncertainty.

Sample Description	Measured Capacity (C_V) ± U	Characteristic Pressure Ratio x_{Fz} ± U
Maximized ϕ_1 device, 0.672 Target C_V	0.592 ± 0.006	>0.865 ± 0.011
Maximized ϕ_1 device, 0.96 Target C_V	0.914 ± 0.008	0.824 ± 0.011
Maximized ϕ_1 device, 1.248 Target C_V	1.076 ± 0.010	0.752 ± 0.010
Maximized ϕ_2 device, 0.96 Target C_V	1.007 ± 0.008	0.727 ± 0.010

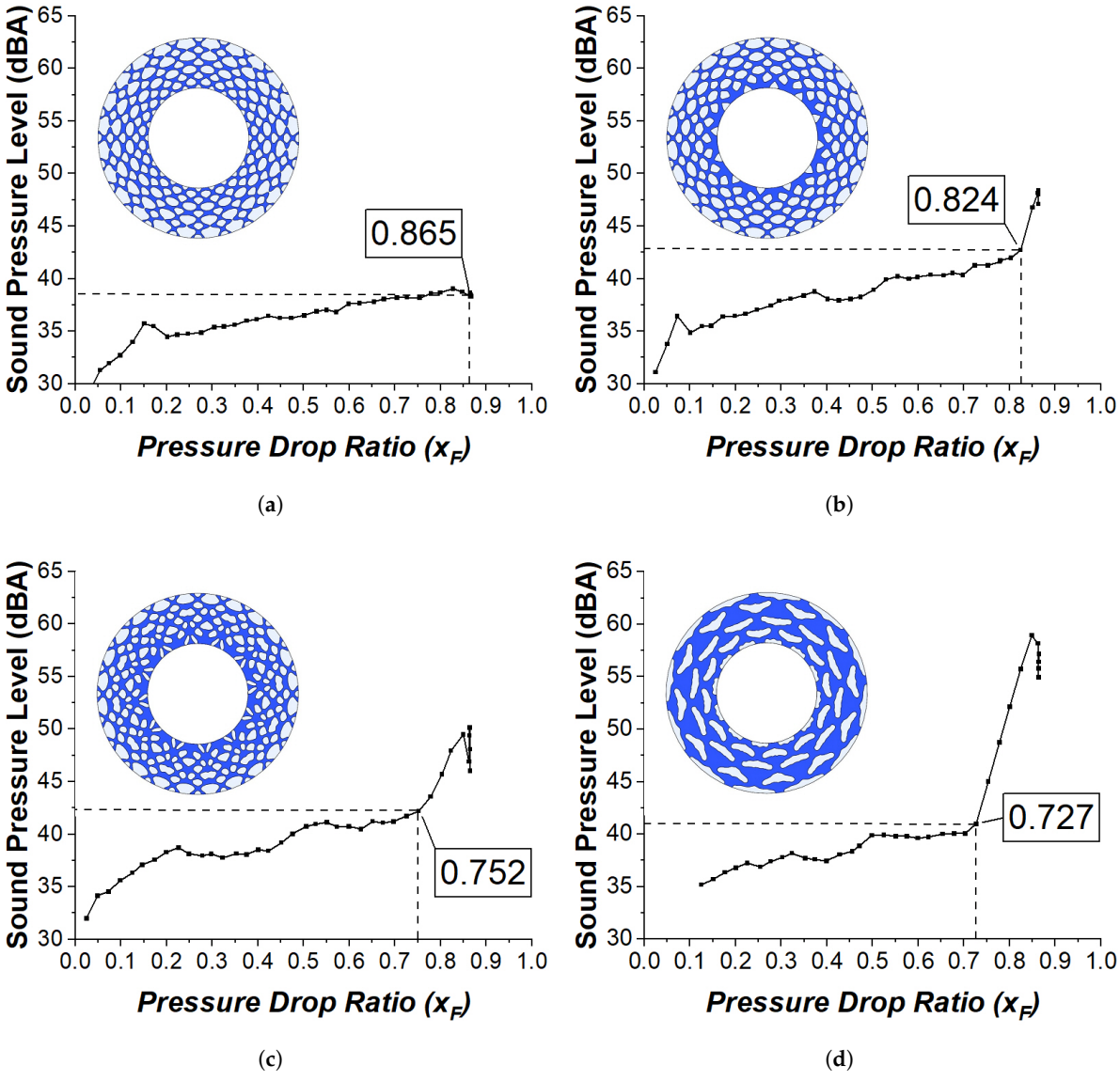


Figure 12. Static pressure fields, scaled for low pressure contrast. (**a**) Maximized ϕ_1 device, 0.672 nominal capacity. (**b**) Maximized ϕ_1 device, 0.96 nominal capacity. (**c**) Maximized ϕ_1 device, 1.248 nominal capacity. (**d**) Maximized ϕ_2 device, 0.96 nominal capacity.

3.5. Comparison of 2D and 3D Hard Boundary Simulation Performance

Given that the physical testing results of two of the design cases slightly exceeded the industry's 10% error allowable norm (at 12% and 14%), a short investigation was performed to determine whether substitution of 3D simulation for the 2D simulation in the hard-boundary evaluation process step (see Figure 2) would reduce error in all test cases to acceptable values. To this end, steady-state simulations with a realizable $k-\epsilon$ turbulence model (enhanced wall treatment, $\sigma_k = 1$, $C_{2\epsilon} = 1.9$, $\sigma_\epsilon = 1.2$) were run on the extruded 2D hard-boundary geometries, using the same boundary conditions, in Ansys Fluent 2024 (R2) [34]. Mesh settings are shown in Table 8. These settings were sufficiently refined to keep the wall y^+ at or below unity for most areas (the maximum wall y^+ in the simulations was 1.25); additionally, a mesh sensitivity study showed a deviation of less than 0.3% in C_V vs. the reference mesh simulation with a 20% mesh refinement (min cell size, number of cells per gap).

The results of these flow simulations (see Table 9) revealed much better adherence to the laboratory test results, with a maximum 3D capacity error vs. test of 7.8%. Examining the velocity flow field of the ϕ_1 objective (nominal capacity of 0.96) along the middle plane of the 3D simulation, Figure 13, shows similar flow behavior to the 2D analysis (Figure 8b) with the caveat that velocities do not taper downward as quickly as the flow moves radially toward the exit. To better characterize and compare this behavior, the maximum channel velocity along the radial dimension of this same device was plotted (see Figure 14) for both the 2D and 3D mid-plane simulations. These plots also showed increased stream cohesion at the exit, represented by a higher device outlet maximum velocity. Given the increased conformance to capacity test results, it is recommended that a 3D model be used in the workflow to define the optimization output final filter parameter.

Table 8. Three-Dimensional Simulation Mesh Settings.

Min Size (mm)	Max Size (mm)	Growth Rate	Size Funct.	Curv. Norm Angle (deg.)	Cells per Gap	B. Layers (BL)
0.015	0.09	1.2	Curv. and Prox.	18	15	10

Table 9. 3D Simulation Analysis Results.

Sample Description	Capacity (C_V)	Min Element Pressure (Pa)	Max Element Velocity (m/s)
Maximized ϕ_1 device, 0.672 Target C_V	0.619	−665.6	2.75
Maximized ϕ_1 device, 0.96 Target C_V	0.922	−1039.0	3.39
Maximized ϕ_1 device, 1.248 Target C_V	1.160	−2098.6	3.78
Maximized ϕ_2 device, 0.96 Target C_V	0.974	−3715.9	3.77

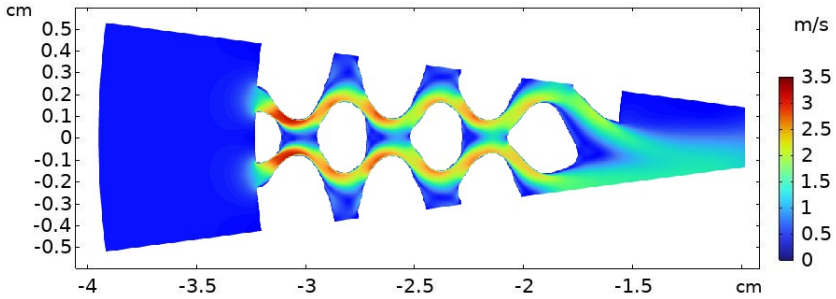


Figure 13. ANSYS Fluent 3D simulation velocity plot of channel center plane, $C_V = 0.96$ ϕ_1 device.

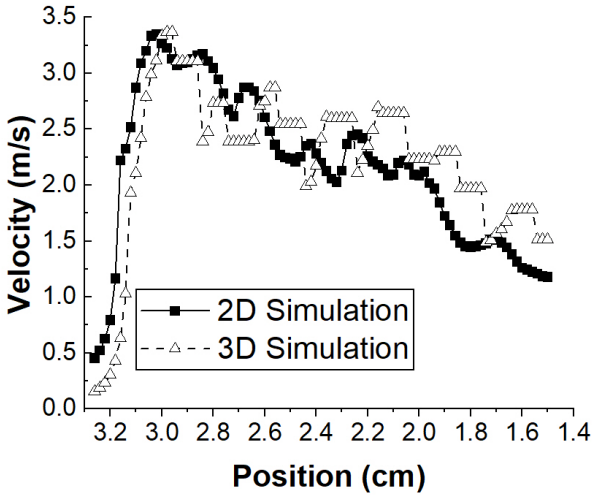


Figure 14. Comparison of radial position maximum channel velocities for the nominal capacity $C_V = 0.96\,\phi_1$ device, 2D vs. 3D.

3.6. Results Summary

The results described in this section can be summarized briefly as follows:

- The geometries generated, analyzed, fabricated, and tested using the methods described in this work demonstrated both required capacity specificity and robust pressure staging behavior, successfully minimizing the static pressure in the surrounding channel at locations of potential cavitation.
- The methods shown in this work are capable of quantitatively comparing the effectiveness of proposed objective functions to generate cavitation suppression designs, as is demonstrated by the contrast in x_{FZ} values between the equivilent-capacity ϕ_1 and ϕ_2 designs.
- The intuitive correlation between decreased non-uniform hydraulic diameter and increased cavitation suppression was supported by testing. We will formalize this relationship in a future work on pressure staging theory.
- Optimization geometry results were scaled for fabrication and deployment in a full-size globe valve (ANSI 2-inch).
- With an added 3D tuning step (2D/3D hybrid model), capacity accuracy within the tested valve are within industry norms of $\pm 10\%$ (the maximum error between the physical test results and the 3D model was 7.8%).
- Optimization parameter and mesh sensitivity studies demonstrated robustness and mesh insensitivity at chosen settings.

4. Conclusions

This work demonstrated a complete reduction-to-practice of a design method for the production of capacity-specific radial control valve anti-cavitation trim using density-based topology optimization. The approach used directional change maximization objectives in conjunction with a standardized turbulent control valve capacity formulation to design components for high pressure drop applications. Currently, this is the only method existing which generates capacity-specific freeform valve trim.

Using density-based TO with velocity and pressure drop constraints, we generated and subsequently fabricated four control valve trim designs of various capacities and evaluated their performance using simulations and flow testing in water. Two objective functions and three capacities were evaluated by examining the number, location, and extent of low pressure regions in a simulated flow domain for a given system pressure differential; all

designs were then fabricated using low-cost (approximately USD 45 per sample) masked stereolithography and tested in water to measure capacity and acoustically determine their cavitation suppression performance. The x-directional velocity objective function (ϕ_1) was found to be stable and highly effective, achieving a measured cavitation initiation measurement x_{Fz} in excess of 0.86, and demonstrating a worst-case measurement of installed capacity 4% outside the industry accuracy guidelines using a fully 2D based procedure. Replacing the hard-boundary 2D simulations with a resolved 3D simulation further reduces the test inaccuracy to well within acceptable limits.

This method is expected to greatly speed industrial severe service solutions in situations where high performance and speed are critical, such as refinery and power plant applications, where a failed valve can halt the operation of an entire facility. In contrast to parametric design methods that require maintaining libraries of over 1400 unique flow geometries per product line (conservatively, considering ANSI sizes 0.5 through 8 inch, pressure class 150 through 1500, 10% capacity resolution and two flow characteristics), the TO framework generates a capacity-specific design in a single optimization run, with fabrication-ready geometry available within 2–3 days. Using the methods described above allows generated designs to be rapidly printed on-site using additive manufacturing and deployed in days, rather than weeks, and may be redesigned for changed application requirements with the modification of a single parameter if used after proper model tuning to account for the wall surface roughness of the chosen manufacturing method. In addition, exploration of the method will allow for the generation of designs with specific functional characteristics and physics-driven objectives, which can be generated and evaluated at dramatically reduced cost vs. the prior art's imposition of geometric features and subsequent parametric modification.

Author Contributions: The authors B.B., J.A. and S.R. conceived the approach taken in this work, planned, and modified (as necessary) the methodology, and participated in the creation of the visualizations presented here. B.B. performed the described simulations and experiments, with numerical simulation concept and implementation support from J.A. and experimental method and conceptual support from S.R., B.B. took the lead in writing the manuscript, with all authors discussing the results and contributing to the final manuscript. All authors have read and agreed to the published version of the manuscript.

Funding: This work was supported by Flowserve Corporation and the University of Utah. Joe Alexandersen did not receive funding for his contribution.

Institutional Review Board Statement: Not applicable.

Informed Consent Statement: Not applicable.

Data Availability Statement: Additional data supporting the conclusions of this article are available upon reasonable request.

Conflicts of Interest: Bruce Butler is currently employed by Flowserve Corporation. The funders had no role in the design of the study; in the collection, analyses, or interpretation of data; in the writing of the manuscript; or in the decision to publish the results.

References

1. Hammitt, F.G. *Cavitation and Multiphase Flow Phenomena*, 1st ed.; McGraw-Hill: Columbus, OH, USA, 1980; p. 423.
2. Young, F.R. *Cavitation*, 2nd ed.; McGraw-Hill: Columbus, OH, USA, 1999; p. 418.
3. Sigmund, O.; Maute, K. Topology optimization approaches: A comparative review. *Struct. Multidiscip. Optim.* **2013**, *48*, 1031–1055. [CrossRef]
4. Deaton, J.D.; Grandhi, R.V. A survey of structural and multidisciplinary continuum topology optimization: Post 2000. *Struct. Multidiscip. Optim.* **2014**, *49*, 1–38. [CrossRef]

5. Bendsøe, M.P.; Kikuchi, N. Generating optimal topologies in structural design using a homogenization method. *Comput. Methods Appl. Mech. Eng.* **1988**, *71*, 197–224. [CrossRef]
6. Bendsøe, M.; Sigmund, O. *Topology Optimization: Theory, Methods, and Applications*; Springer: Berlin/Heidelberg, Germany, 2002. [CrossRef]
7. Borrvall, T.; Petersson, J. Topology optimization of fluids in Stokes flow. *Int. J. Numer. Methods Fluids* **2003**, *41*, 77–107. [CrossRef]
8. Gersborg-Hansen, A.; Sigmund, O.; Haber, R.B. Topology optimization of channel flow problems. *Struct. Multidiscip. Optim.* **2005**, *30*, 181–192. [CrossRef]
9. Olesen, L.H.; Okkels, F.; Bruus, H. A high-level programming-language implementation of topology optimization applied to steady-state Navier-Stokes flow. *Int. J. Numer. Methods Eng.* **2006**, *65*, 975–1001. [CrossRef]
10. Othmer, C. A continuous adjoint formulation for the computation of topological and surface sensitivities of ducted flows. *Int. J. Numer. Methods Fluids* **2008**, *58*, 861–877. [CrossRef]
11. Kontoleontos, E.A.; Papoutsis-Kiachagias, E.M.; Zymaris, A.S.; Papadimitriou, D.I.; Giannakoglou, K.C. Adjoint-based constrained topology optimization for viscous flows, including heat transfer. *Eng. Optim.* **2013**, *45*, 941–961. [CrossRef]
12. Yoon, G.H. Topology optimization for turbulent flow with Spalart–Allmaras model. *Comput. Methods Appl. Mech. Eng.* **2016**, *303*, 288–311. [CrossRef]
13. Dilgen, C.B.; Dilgen, S.B.; Fuhrman, D.R.; Sigmund, O.; Lazarov, B.S. Topology optimization of turbulent flows. *Comput. Methods Appl. Mech. Eng.* **2018**, *331*, 363–393. [CrossRef]
14. Yoon, G.H. Topology optimization method with finite elements based on the k-ϵ turbulence model. *Comput. Methods Appl. Mech. Eng.* **2020**, *361*, 112784. [CrossRef]
15. Alexandersen, J.; Andreasen, C.S. A Review of Topology Optimisation for Fluid-Based Problems. *Fluids* **2020**, *5*, 29. [CrossRef]
16. Hanimann, L.; Mangani, L.; Casartelli, E.; Widmer, M. Cavitation modeling for steady-state CFD simulations. *IOP Conf. Ser. Earth Environ. Sci.* **2016**, *49*, 092005. [CrossRef]
17. Ferrarese, G.; Messa, G.V.; Rossi, M.M.; Malavasi, S. New method for predicting the incipient cavitation index by means of single-phase computational fluid dynamics model. *Adv. Mech. Eng.* **2015**, *7*, 1687814015575974. [CrossRef]
18. Tang, T.; Gao, L.; Li, B.; Liao, L.; Xi, Y.; Yang, G. Cavitation optimization of a throttle orifice plate based on three-dimensional genetic algorithm and topology optimization. *Struct. Multidiscip. Optim.* **2019**, *60*, 1227–1244. [CrossRef]
19. Butler, B.J.; Alexandersen, J.; Rao, S.R. Experimental Demonstration of a Topology Optimization Method to Generate a Capacity-Specific Device With Cavitation Resistance for Control Valve Applications. *ASME J. Fluids Eng.* **2025**, *147*, 051503. [CrossRef]
20. *IEC 60534-8-2:2011*; Noise Considerations—Laboratory Measurement of Noise Generated by Hydrodynamic Flow Through Control Valves. Technical Report. IEC: Geneva, Switzerland, 2011.
21. *IEC 60534-2-3:2015*; Industrial-Process Control Valves—Part 2–3: Flow Capacity—Test Procedures. IEC: Geneva, Switzerland, 2018.
22. NIST. *NIST Standard Reference Database 23*; NIST: Gaithersburg, MD, USA, 2010.
23. Weiwei, J. Derivation of "Double-Loop" Theory and Mechanism of Cavitation-Vortex Interaction in Turbulent Cavitation Boundary Layer. *J. Fluids Eng. Trans. ASME* **2024**, *146*, 094501. [CrossRef]
24. Pérali, P.; Hauville, F.; Leroyer, A.; Astolfi, J.A.; Visonneau, M. Experimental and Numerical Study of the Flow Around Rigid and Flexible Hydrofoils for Wetted and Cavitating Flow Conditions. *J. Fluids Eng. Trans. ASME* **2024**, *146*, 111201. [CrossRef]
25. Malavasi, S.; Messa, G.V.; Fratino, U.; Pagano, A. On cavitation occurrence in perforated plates. *Flow Meas. Instrum.* **2015**, *41*, 129–139. [CrossRef]
26. *CFD Module User's Guide*; COMSOL Multiphysics v. 6.3; COMSOL AB: Stockholm, Sweden, 2023; pp. 242–245.
27. Alexandersen, J. Topography optimisation of fluid flow between parallel plates of spatially-varying spacing: Revisiting the origin of fluid flow topology optimisation. *Struct. Multidiscip. Optim.* **2022**, *65*, 152. [CrossRef]
28. Kuzmin, D.; Mierka, O.; Turek, S. On the implementation of the $k-\varepsilon$ turbulence model in incompressible flow solvers based on a finite element discretisation. *Int. J. Comput. Sci. Math.* **2007**, *1*, 193–206. [CrossRef]
29. *Optimization Module User's Guide*; COMSOL Multiphysics v. 6.0; COMSOL AB: Stockholm, Sweden, 2023.
30. Lazarov, B.S.; Sigmund, O. Filters in topology optimization based on Helmholtz-type differential equations. *Int. J. Numer. Methods Eng.* **2010**, *86*, 765–781. [CrossRef]
31. Svanberg, K. A Class of Globally Convergent Optimization Methods Based on Conservative Convex Separable Approximations. *SIAM J. Optim.* **2002**, *12*, 555–573. [CrossRef]
32. Tano, I.N.; Rasouli, E.; Seo, J.; Raikar, S.; Hildreth, O.; Rollett, A.; Narayanan, V. The Influence of Model Orientation on the Surface Roughness of Polymeric Models Produced by FFF, mSLA, PJ, and SLS Methods. *Materials* **2025**, *18*, 5600. [CrossRef] [PubMed]
33. Singh, D.; Charlton, M.; Asim, T.; Mishra, R.; Townsend, A.; Blunt, L. Quantification of additive manufacturing induced variations in the global and local performance characteristics of a complex multi-stage control valve trim. *J. Pet. Sci. Eng.* **2020**, *190*, 107053. [CrossRef]
34. *ANSYS Fluent Theory Guide*; Release 2024 R2; ANSYS, Inc.: Canonsburg, PA, USA, 2024.

35. Coleman, H.; Steele, W.G. *Experimentation, Validation, and Uncertainty Analysis for Engineers*, 4th ed.; Wiley: Hoboken, NJ, USA, 2018. [CrossRef]
36. Bazan, A.; Turek, P.; Budzik, G.; Niesłony, P.; Grygoruk, R.; Siemiński, P. Assessment of the relative impacts of feature accuracy and surface roughness on fluid flow across additively manufactured pin arrays. *Therm. Sci. Eng. Prog.* **2025**, *64*, 103769. [CrossRef]
37. Emswiler, G.; Hoyme, M. How Additive Manufacturing Leads to Quieter Control Valves. *InTech (ISA)*, 29 April 2023.

Disclaimer/Publisher's Note: The statements, opinions and data contained in all publications are solely those of the individual author(s) and contributor(s) and not of MDPI and/or the editor(s). MDPI and/or the editor(s) disclaim responsibility for any injury to people or property resulting from any ideas, methods, instructions or products referred to in the content.